ADVANCED MATERIALS
www.advmat.de

Room-Temperature Anode-Less All-Solid-State Batteries via the Conversion Reaction of Metal Fluorides

Jieun Lee, Seung Ho Choi, Gahyeon Im, Kyu-Joon Lee, Taegeun Lee, Jihoon Oh, Nohjoon Lee, Hyuntae Kim, Yunsung Kim, Sangheon Lee, and Jang Wook Choi**

All-solid-state batteries (ASSBs) that employ anode-less electrodes have drawn attention from across the battery community because they offer competitive energy densities and a markedly improved cycle life. Nevertheless, the composite matrices of anode-less electrodes impose a substantial barrier for lithium-ion diffusion and inhibit operation at room temperature. To overcome this drawback, here, the conversion reaction of metal fluorides is exploited because metallic nanodomains formed during this reaction induce an alloying reaction with lithium ions for uniform and sustainable lithium (de)plating. Lithium fluoride (LiF), another product of the conversion reaction, prevents the agglomeration of the metallic nanodomains and also protects the electrode from fatal lithium dendrite growth. A systematic analysis identifies silver (I) fluoride (AgF) as the most suitable metal fluoride because the silver nanodomains can accommodate the solid-solution mechanism with a low nucleation overpotential. AgF-based full cells attain reliable cycling at 25 °C even with an exceptionally high areal capacity of 9.7 mAh cm^{-2} (areal loading of $LiNi_{0.8}Co_{0.1}Mn_{0.1}O_2$ = 50 mg cm^{-2}). These results offer useful insights into designing materials for anode-less electrodes for sulfide-based ASSBs.

1. Introduction

All-solid-state batteries (ASSBs) have been attracting considerable interest as promising alternatives to the lithium-ion batteries (LIBs) that are currently in use, especially in view of their enhanced safety.[1] Thus far, research in this area has made a substantial progress in identifying various superionic conductors belonging to the oxide, sulfide, and halide families.[2] Among these families, sulfide solid electrolytes (SEs) have been considered one of the most feasible options owing to their high lithium (Li)-ion conductivities and good mechanical properties.[3] Remarkably, the sulfide SEs $Li_{6.6}Si_{0.6}Sb_{0.5}S_5I$,[4] $Li_{9.54}Si_{1.74}P_{1.44}S_{11.7}Cl_{0.3}$,[5] and $Li_{10}GeP_2S_{12}$[6] exhibit ionic conductivities of the order of 10^{-2} S cm^{-1}, i.e., at the level of commercial liquid electrolytes. From a mechanics viewpoint, the intrinsic ductileness of sulfide SEs enables them to build intimate contacts with active materials by simple cold pressing, unlike oxide SEs that do not usually form continuous ion percolation paths even after high-temperature sintering. In particular, the argyrodites Li_6PS_5X (X = Cl, Br, and I) stand at the center of research pertaining to sulfide-based ASSBs owing to the low cost of their precursors and the simple synthesis method, in addition to the aforementioned electrochemical and mechanical advantages of sulfide SEs.[7]

ASSBs also offer potentially high energy density.[8] In contrast to the conventional liquid-based LIBs, ASSBs can adopt the bipolar stacking of electrodes in a single cell to achieve a serial cell connection, which substantially reduces the packaging weight and volume.[9] Furthermore, ASSBs are widely accepted to raise the possibility of using metallic Li as an anode.[10] Metallic Li is the ultimate anode material in terms of energy density because it has the highest theoretical capacity of 3860 mAh g^{-1} and the lowest electrochemical potential of −3.04 V versus the standard hydrogen electrode. However, the limited Coulombic efficiency (CE) that arises from continuous electrolyte decomposition along with indiscriminately grown Li dendrites has impeded the progress of lithium metal batteries.[11] Although the solid nature of sulfide SEs may be more beneficial for combating Li dendrite growth compared to liquid electrolytes, the development of sustainable all-solid-state lithium metal batteries remains nontrivial. This is because of the poor reductive stability of sulfide SEs and the internal short circuits caused by the inevitable defects within the SE layer when external pressure is applied during cell fabrication or operation.[12] Although some SEs demonstrated reversible Li (de)plating during cycling by forming a stable solid electrolyte interphase (SEI) on Li metal foil,[13] uncontrolled dendrite growth and subsequent penetration of the SE layer

J. Lee, T. Lee, J. Oh, N. Lee, H. Kim, J. W. Choi
School of Chemical and Biological Engineering and
Institute of Chemical Processes
Seoul National University
1 Gwanak-ro, Gwanak-gu, Seoul 08826, Republic of Korea
E-mail: jangwookchoi@snu.ac.kr

S. H. Choi, G. Im, K.-J. Lee, Y. Kim, S. Lee
Advanced Battery Development Team
Hyundai Motor Company
150, Hyundaiyeonguso-ro, Namyang-eup, Hwaseong-si
Gyeonggi-do 18280, Republic of Korea
E-mail: sheonlee@hyundai.com

J. W. Choi
Department of Materials Science and Engineering
Seoul National University
1 Gwanak-ro, Gwanak-gu, Seoul 08826, Republic of Korea

The ORCID identification number(s) for the author(s) of this article can be found under https://doi.org/10.1002/adma.202203580.

DOI: 10.1002/adma.202203580

remain a formidable challenge for all-solid-state lithium metal batteries.[14] The "anode-less" concept has recently emerged as an alternative option to Li metal foil and is referred to as a Li storage mechanism without an intercalation host.[15] In this concept, no intercalation host is present in the initial cell configuration; only a current collector exists. Because the cell is fabricated with an "empty" anode layer, high energy density can be targeted along with simplified cell fabrication. Furthermore, a recent study[16] demonstrated a robust cycle life exceeding 1000 cycles by incorporating a silver (Ag)–carbon composite layer. In this layer, silver serves as a nucleation seed in the alloying reaction with Li to afford more uniform and controllable Li plating without initiating dendrites. Unfortunately, however, the given anode-less cell could not operate at room temperature because of the limited kinetics in terms of Li-ion diffusion through the composite layer, leaving room for further advancement before the anode-less ASSB is established as a more practical technology.

Here we report anode-less ASSBs that operate at room temperature by implementing conversion-type metal fluoride (MF_x). The conversion reaction of metal fluoride with Li produces lithium fluoride (LiF) following which the metal M proceeds to form the lithium–metal alloy (Li–M), in this sequence. Hence, the anode-less composite layer is protected by LiF while the alloying reaction promotes uniform Li plating for which the metal serves as a nucleation seed. We assessed various metal fluorides and found that the Li plating kinetics and behavior are largely affected by the Li–M reaction mechanism. Considering that a solid-solution reaction that imposes a lower nucleation barrier is more desirable for facile and uniform Li plating, silver (I) fluoride (AgF) is advantageous compared with other metal fluorides. Meanwhile, the electronically insulating LiF mitigates the reduction of the sulfide SE by blocking electronic transport toward stabilizing the interface and suppresses Li dendrite growth.[10c] The current investigation reveals the importance of understanding the reaction mechanism and relevant kinetics regarding the storage of Li in the anode-less composite layer for realizing anode-less ASSBs based on sulfides and that operate reliably at room temperature.

2. Results and Discussion

2.1. Lithium Nucleation on Conversion-Type Metal Fluorides

The in situ conversion reaction of metal fluorides (MF_x, M = Ag, Sn(II), In, Zn, Bi, Al, Sn(IV), Mg, Ca, Cs) was investigated in asymmetric MF_x|SE|Li all-solid-state half-cells (**Figure 1**; Figure S1, Supporting Information). The metal fluoride undergoes sequential conversion and alloying reactions[17]

$$x\mathrm{Li} + \mathrm{MF}_x \rightarrow \mathrm{M} + x\mathrm{LiF} \quad (1)$$

$$\mathrm{Li} + \mathrm{M} \rightarrow \mathrm{Li-M} \quad (2)$$

Although all of the metal fluorides listed above are well-known conversion materials for LIBs,[17,18] only AgF, indium fluoride (InF_3), tin(II) fluoride (SnF_2), zinc fluoride (ZnF_2), and bismuth fluoride (BiF_3) exhibited conversion behavior in our ASSB tests at 25 °C (Figure 1a; Figure S1a, Supporting Information). As each pristine anode-less composite layer consisted only of the metal fluoride, of which the electronic conductivity is relatively low, and poly(vinylidene difluoride) (PVDF) binder, the kinetics of the conversion reaction of the metal fluoride was highly restricted by the bonding characteristics between the metal and fluorine. For these tests, anode-less electrodes with an areal loading of 0.25 mg cm^{-2} were prepared by casting metal-fluoride-containing slurry onto stainless steel (SUS) foil (details of the procedure appear in the "Experimental Section"). Notably, the conversion and subsequent alloying reactions are feasible at room temperature such that the overall Li plating can be completed at room temperature. This lithiation behavior contrasts that of the Ag–carbon composite, which requires the temperature to be raised to overcome the diffusion barrier in the carbon matrix.[16] On the other hand, side reactions accompanied by the reduction of the solid electrolyte can be avoided by the formation of insulating LiF from the conversion reaction. When Li was plated at a current density of 1 mA cm^{-2}, AgF-, SnF_2-, InF_3-, ZnF_2-, and BiF_3-based electrodes exhibited gradual slopes in the beginning of lithiation in reflection of the conversion reaction, followed by voltage plateaus corresponding to Li plating involving the alloying reaction (Figure 1a; Figure S1a, Supporting Information). In contrast to these metal fluorides, the potential profiles of aluminum fluoride (AlF_3)-, tin(IV) fluoride (SnF_4)-, magnesium fluoride (MgF_2)-, calcium fluoride (CaF_2)-, and cesium fluoride (CsF)-based electrodes dropped immediately once lithiation commenced, indicating that the conversion reaction of these metal fluorides is not feasible (Figure 1b; Figure S1c, Supporting Information). Although metallic Al, Sn, Mg, and Ca can alloy with lithium, the alloying reaction of AlF_3, SnF_4, MgF, and CaF_2 was infeasible because the preceding conversion reaction was unavailable. Interestingly, the Sn(II)F_2- and Sn(IV)F_4-based electrodes behaved differently despite both having tin as the central metal, owing to sluggish anion diffusivity in the cation matrix of Sn^{4+}. The series of results indicate that the conversion trend depends largely on the M−F bonding nature. Those with high-atomic-number metals (e.g., AgF, InF_3, ZnF_2, and BiF_3) are feasible for conversion reaction whereas those with low-atomic-number or alkali (earth) metals (e.g., AlF_3, MgF_2, CaF_2, and CsF) are not owing to their high bonding strength between metal and fluorine. The difference between SnF_2 and SnF_4 can also be explained by the same logic; Sn with the higher oxidation state forms the stronger bond with F.

The reaction kinetics is also affected by the alloying reaction (reaction (2) above), particularly in relation to its nucleation energy barrier whose magnitude is reflected in the difference between the dip and the plateau on the enlarged potential profile (Figure 1c,d; Figure S1b,d, Supporting Information). This difference can be referred to as nucleation overpotential. According to this metric, AgF-, SnF_2-, InF_3-, ZnF_2-, and BiF_3-based electrodes had nucleation overpotentials of 0.92, 3.1, 2.6, 3.4, and 10 mV, respectively, implying that AgF is the most efficient in terms of nucleating the Li–M alloy. In sharp contrast, the AlF_3-, SnF_4-, MgF_2-, CaF_2-, and CsF-based electrodes did not exhibit any alloying behavior at all because the conversion reaction that produces metallic (M^0) domains was unavailable. Thus, Li plating on those

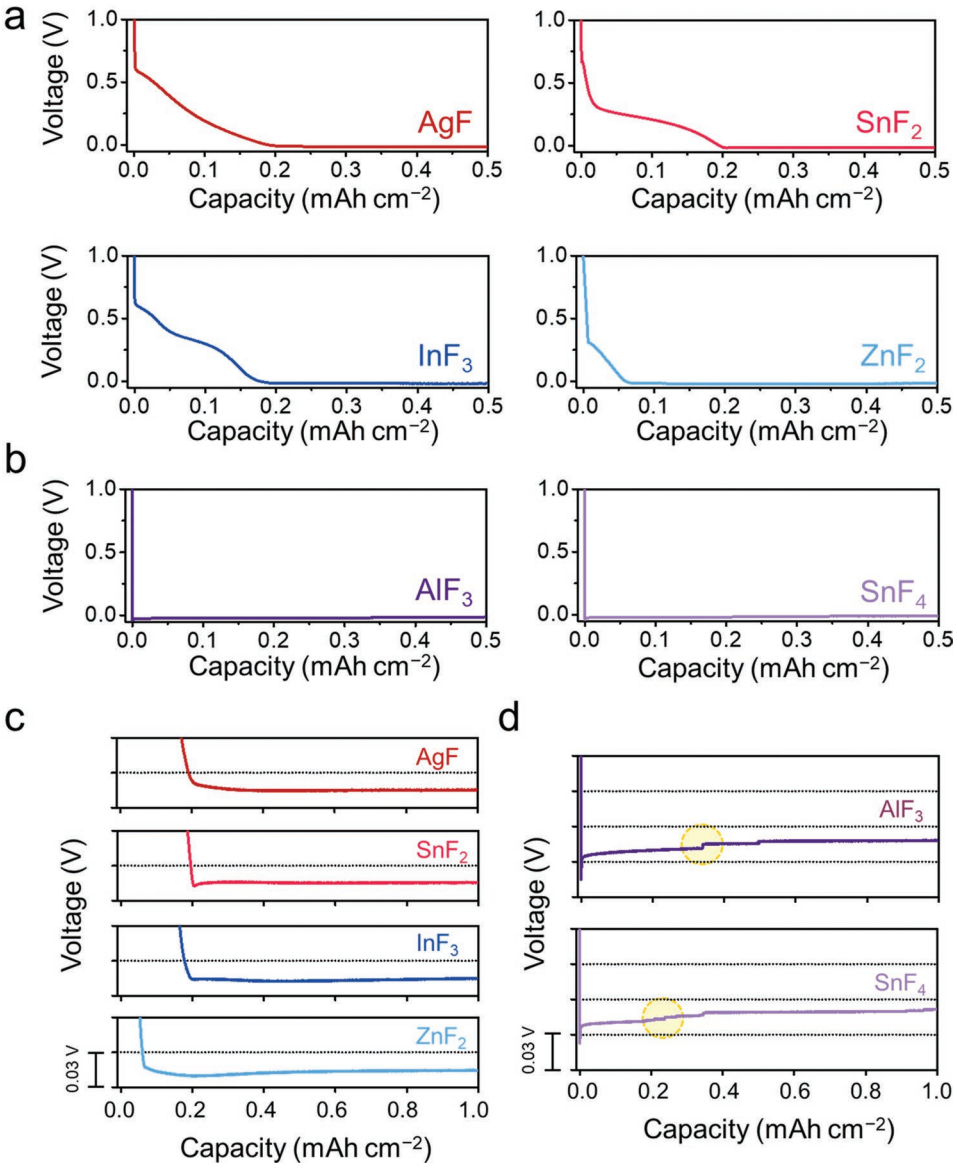

Figure 1. Conversion of various metal fluorides during Li plating. a) Galvanostatic voltage profiles during Li plating on the electrodes containing AgF, SnF_2, InF_3, ZnF_2 when scanned at a current density of 1 mA cm^{-2} at 25 °C. b) Galvanostatic voltage profiles during Li plating on the electrodes containing AlF_3 and SnF_4 with a current density of 1 mA cm^{-2} at 25 °C. c,d) The same profiles as panels (a) and (b), respectively, but in different voltage and capacity scales. The dashed yellow circles indicate soft shorting.

electrodes did not involve heteroatoms but rather imposed far higher nucleation energy barrier, which was reflected in the higher initial overpotentials. Moreover, when the Li plating profiles were viewed at high magnification (Figure 1d; Figure S1d, Supporting Information), sudden increases were observed (marked with yellow circles) on the voltage plateaus. These increases are indicative of soft shorting, even after the small amount of plating of 0.3 mAh cm^{-2}, which originated from irregular Li plating in the absence of the alloying reaction. Similarly, control cases prepared by plating Li on the LiF-based electrode and bare SUS substrate (Figure S2, Supporting Information) experienced immediate voltage drop in the beginning, because a metal was not present for the conversion reaction.

2.2. Characterization of Metal Fluorides upon Lithiation

The chemical compositions and structural changes of AgF and InF_3 upon lithiation were examined by X-ray photoelectron spectroscopy (XPS) and X-ray diffraction (XRD) analyses (**Figure 2**; Figure S3, Supporting Information). For these analyses, AgF|SE|Li and InF_3|SE|Li half-cells were fabricated and galvanostatically charged (lithiated) at a current density of 1 mA cm^{-2} at 25 °C. As expected, the high-resolution Ag 3d spectrum of the pristine AgF electrode was well fitted to two peaks of the pristine AgF, 373.3 eV (Ag $3d_{3/2}$) and 367.3 eV (Ag $3d_{5/2}$). After lithiation, the Ag 3d spectrum was deconvoluted into two main peaks at 373.4 eV (Ag $3d_{3/2}$) and 367.3 eV (Ag $3d_{5/2}$), along with two shoulder peaks at 374.5 eV (Ag $3d_{3/2}$) and 368.4 eV

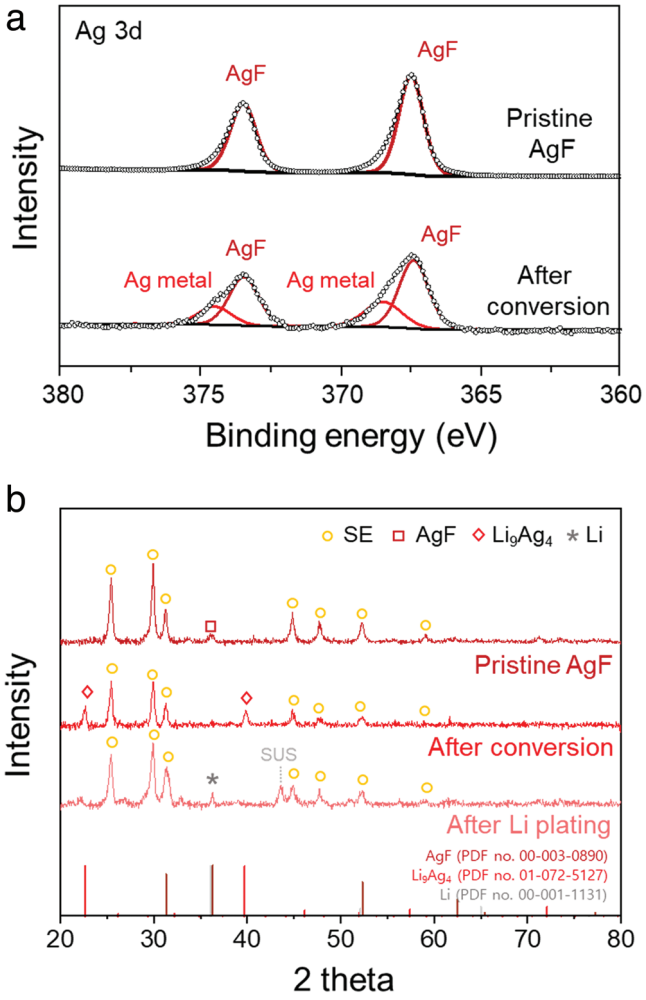

Figure 2. XPS and XRD analyses of metal fluorides upon Li plating. a) High-resolution Ag 3d spectra of (top) pristine and (bottom) lithiated AgF. b) XRD patterns of AgF in the pristine state, and after conversion, after Li metal plating. The characteristic peaks of AgF, Li_9Ag_4, and Li are from ICDD database.

($Ag\ 3d_{5/2}$). The newly appeared shoulder peaks indicate the conversion of AgF to metallic Ag^0, supporting the occurrence of the conversion reaction.[19] Interestingly, the sequence of the Ag and AgF peak positions in the Ag 3d spectrum is opposite to that of their In counterparts that follow the normal trend; typically, the bonding energy of metal halide is larger than that of the metallic one of the corresponding metal. Unfortunately, the reason for the anomalous trend of Ag has remained unidentified for a while.[20] The XRD patterns were characterized by the disappearance of the crystalline AgF peak at 36.3°, and the appearance of Li_9Ag_4 alloy peaks at 22.6° and 39.9° as a result of the conversion reaction when charged to 0 V versus Li^+/Li.[16,21] After further deposition of Li, a Li metal diffraction peak appeared at 36.2°, pointing to the plating of metallic Li^0.[21b] In the case of InF_3, the conversion of InF_3 to metallic In^0 was also confirmed in the high-resolution In 3d spectrum (Figure S3a, Supporting Information). The spectrum of the pristine InF_3 electrode was fitted to its two characteristic peaks at 453.2 eV ($In\ 3d_{3/2}$) and 445.7 eV ($In\ 3d_{5/2}$). After charging, metallic indium peaks at 452.0 eV ($In\ 3d_{3/2}$) and 444.5 eV ($In\ 3d_{5/2}$) indicate their appearance.[22] Consistent with the XPS results, the crystalline InF_3 peaks at 22.8°, 33.0°, and 51.1° disappeared from the XRD patterns (Figure S3b, Supporting Information). Instead, the peaks assigned to $Li_{13}In_3$ alloy appeared at 21.7°, 22.7°, 34.3°, and 37.5° after the conversion reaction.[23] Upon further lithiation, the diffraction peak of Li metal was also observed, commensurate with the AgF case.

2.3. Li Plating onto Various Metal Fluorides

The reversibility of Li plating and stripping was assessed for the four metal fluorides—AgF, SnF_2, InF_3, and ZnF_2—with their conversion capability by applying a current density of 1 mA cm^{-2} and an areal capacity of 3 mAh cm^{-2} at 25 °C (Figure S4, Supporting Information). In the case of the AgF- and InF_3-based electrodes, Li plating and stripping were reversible over 60 h, whereas the SnF_2- and ZnF_2-based electrodes ceased to operate by short-circuiting within 30 h (soft shorting marked with yellow-dashed circles). We anticipate the sustainability of Li plating and stripping to be significantly influenced by the Li–M alloying reaction of choice after the preceding conversion reaction of MF_x. Notably, Ag is known to undergo a solid-solution reaction upon formation of its alloy with Li with a lesser degree of structural change, which turns out to deliver stable voltage profiles during cycling.[24] In contrast, Sn and Zn form intermetallic alloys with Li through a reconstitution reaction; the formation of the alloy creates a phase boundary between the regions in which Li is present and those from which Li is absent, imposing a higher energy penalty for Li ions to progress through the metal domains created as a result of the conversion reaction. This higher reaction barrier that the alloying reaction needs to overcome results in poor cyclability.[21b] Interestingly, although Li–In is known to form an intermetallic compound, the voltage profiles of InF_3-based electrodes were moderately stable, implicating the energy penalty for its intermetallic alloying reaction is relatively low.

The cycling performance with regard to Li plating and stripping was evaluated for the AgF- and InF_3-based half-cells by galvanostatically applying a current density of 1 mA cm^{-2} and an areal capacity of 1 mAh cm^{-2} at 25 °C (**Figure 3**). More specifically, in the first cycle, a constant current of 1 mA cm^{-2} was applied until the voltage became 0 V, and thereafter plating of 1 mAh cm^{-2} was processed at the same current density. In subsequent cycles, only the plating step of 1 mAh cm^{-2} occurred without the initial step down to 0 V as the conversion reaction was negligible. Both cells had stable voltage profiles and maintained CEs of higher than 99.5% after the initial few cycles. Remarkably, the AgF-based half-cell cycled stably for more than 500 h (≈250 cycles) (Figure 3a,d) and exhibited an average CE of 99.7% over the same cycling period. By contrast, the InF_3-based half-cell experienced sudden failure before 165 h (83th cycle) as a result of short-circuiting (see the profiles at the 83th cycle in Figure 3b and inset of Figure 3e), which is attributed to the relatively sluggish intermetallic alloying reaction of Li–In, compared to the solid-solution alloy reaction of Li–Ag. These comparative results implicate that the solid-solution reaction is kinetically favorable for the reaction to progress

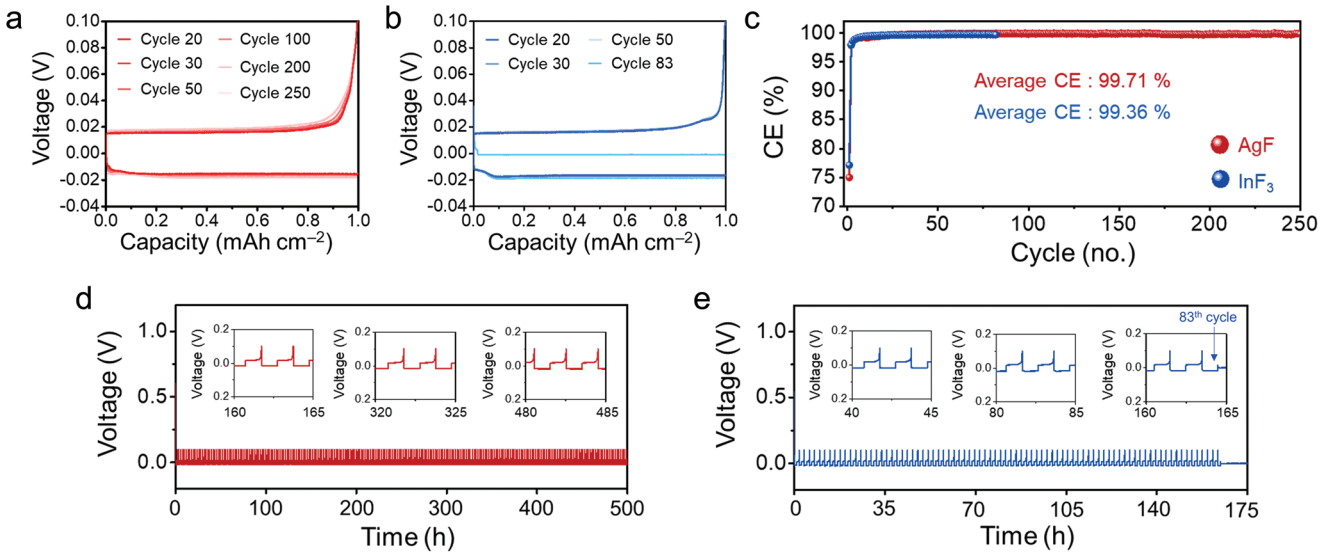

Figure 3. Electrochemical performance of AgF- and InF_3-based ASSB half-cells. Voltage profiles of a) AgF-based and b) InF_3-based MF_x|SE|Li half-cells. Li was plated and stripped at 1 mA cm^{-2} with an areal plating capacity of 1 mAh cm^{-2} at 25 °C. c) Coulombic efficiencies (CEs) of the same cells during cycling. Cycling performance of d) AgF-based and e) InF_3-based half-cells.

and also more effectively releases the stress arising from the volume change of nucleation seeds. Furthermore, the superior cyclability of the AgF-based half-cell was preserved at various current densities of 0.25, 0.5, and 1.5 mA cm^{-2}, and the AgF-based half-cell was sustained for more than 1000, 600, and 400 h, respectively, without any sign of short-circuiting (Figure S5, Supporting Information). The average CEs of the AgF- and InF_3-based electrodes for 250 and 82 cycles were 99.7% and 99.4%, respectively (Figure 3c). The series of results reveals the importance and usefulness of a facile solid-solution alloying reaction to ensure that the anode-less electrode operates reliably with long-term cycling.

2.4. Morphological Changes of AgF-Based Electrodes upon Li Plating and Stripping

Changes in the morphology of the AgF-based electrode were investigated during the plating and stripping of Li metal, by using cross-sectional scanning electron microscopy (SEM) and corresponding energy dispersive X-ray spectroscopy (EDS) analyses (**Figure 4**). In the pristine state (Figure 4a), the elements Ag and F were evenly distributed in the AgF layer located below the SE layer. Note that there was no SUS foil in Figure 4a as the anode-less electrode was transferred onto the SE pellet from an SUS foil when the whole cell assembly was compressed, and the cell assembly was visualized without the SUS plate integrated. After Li plating at a current density of 1 mA cm^{-2} for 5 h, a dense Li metal layer with a thickness of 24 µm was uniformly formed as is evident in Figure 4b. As Ag underwent the alloying reaction with Li, the element Ag was observed throughout the entire region of plated Li as shown in the corresponding EDS image. By contrast, the fluorine remained right beneath the SE layer as in the pristine state, reflecting the interfacial formation of LiF. It is noted that the fluorine signal detected in the SUS foil in Figure 4b,c originated from the X-ray lines of F-Kα and Fe-Lα, which are very close in terms of their energy level. Thus, the given signal is unlikely to indicate the generation of fluorine in the SUS foil. Once Li was stripped from the deposits at the same current density, the Li metal layer disappeared completely with Ag and F again concentrated at the SE–SUS interface.

2.5. Advantage of In Situ Conversion of AgF

Once again, the superiority of AgF as a component of the anode-less electrode arises from its unique features related to the reaction mechanism (**Figure 5**): 1) metallic Ag domains serve as nucleation seeds for uniform and kinetically facile Li plating; and 2) the electronically insulating LiF, the product of the conversion reaction, suppresses dendrite and thus protects the anode-less electrode. The insulating nature of LiF that constitutes the anode matrix also helps prevent the SE from being reduced during charge. To further clarify the reaction mechanism of AgF, galvanostatic Li plating experiments were additionally carried out with electrodes based on Ag and the Ag/LiF mixture (Figure S6, Supporting Information). Unlike the AgF-based electrode, which presented slopes with two separate regimes corresponding to the conversion and alloying reactions (Figure 1a), the Ag-based electrode exhibited only one gradual slope, that of the alloying reaction, as expected (Figure S6a, Supporting Information). Measurements at a much lower current density of 0.1 mA cm^{-2} revealed the difference in the voltage profiles between the two cases more prominently (Figure S7, Supporting Information). Monitoring the Li plating profiles of the three electrodes enables their distinct behaviors to be unraveled, particularly with regard to the Li nucleation overpotential (Figure S8a, Supporting Information). In the first cycle, the profile of the Ag-based electrode showed a small but observable dip in the very early period of Li plating, unlike the other two cases, which originated from the agglomeration of Ag

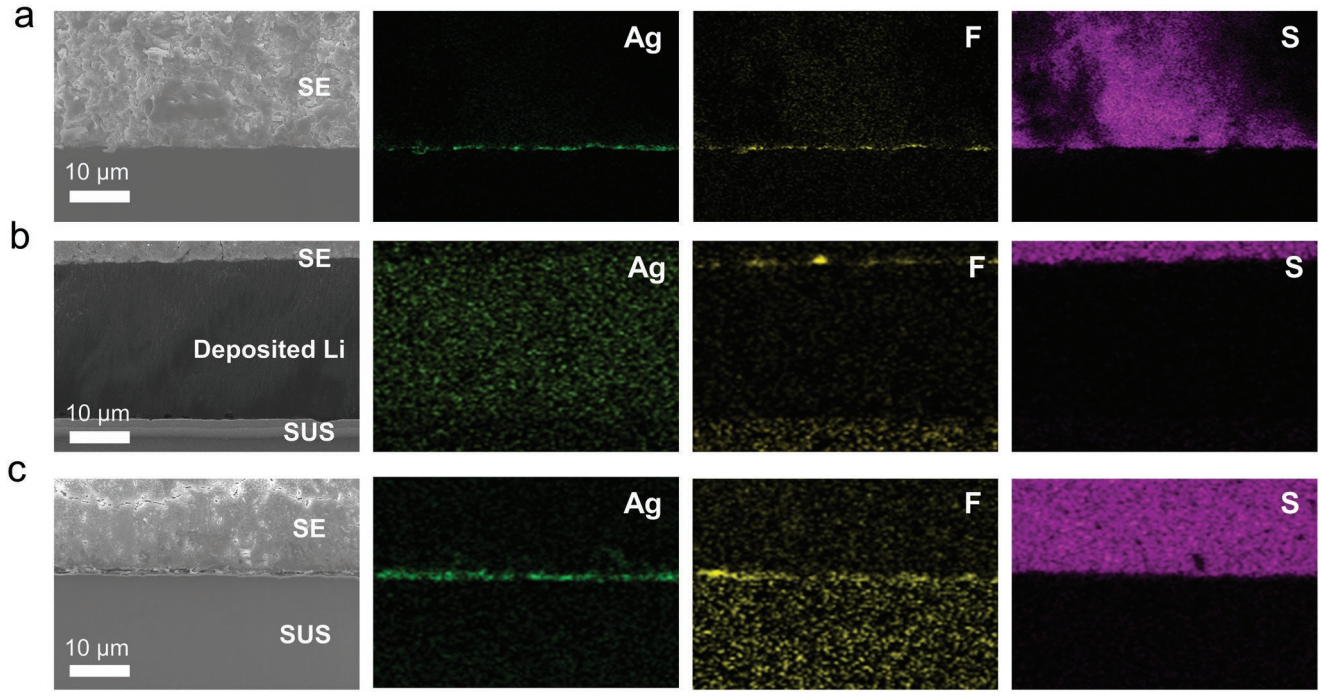

Figure 4. Cross-sectional SEM and corresponding EDS images of AgF-based electrode a) in the pristine state, b) after Li plating, and c) after Li stripping.

particles that impose a barrier for Li-ion diffusion. The voltage profiles evolved in a different manner with cycling (Figure S8b, Supporting Information); the dip in the profile of the Ag-based electrode deepened, and the profile of the Ag/LiF-based electrode began to show a dip, whereas a dip was not apparent on the profile of the AgF-based electrode. These comparative results reflect that the Ag nanodomains formed during the conversion reaction of AgF are more resistant against aggregation by taking advantage of the LiF that is produced as a co-product. The main difference between AgF and Ag/LiF mixture arises from the structures in the original materials. In the case of AgF, Ag nanodomains are formed from the Ag—F bonds of AgF so that their formation is chemically rooted[25] in the matrix of amorphous LiF (Figure S9, Supporting Information). By contrast, Ag in the Ag/LiF mixture does not have any chemical binding with LiF at all in the beginning so that Ag is vulnerable to agglomeration when it becomes mobile. The separated Ag and LiF particles in the Ag/LiF mixture were observed in its pristine state (Figure S10, Supporting Information). The Ag nanodomains are therefore more suitable for uniform and sustainable Li (de)plating over cycling. The aggregation of Ag particles can be understood such that during cycling, when the cell is under pressure, Ag particles tend to diffuse and aggregate via the so-called Oswald ripening,[21] raising the energy barrier for Li nucleation and weakening the role of Ag as a nucleation agent. This phenomenon could be avoided in the case of AgF because the Ag nanodomains that naturally formed from the conversion reaction were most effectively distributed by being surrounded by LiF. Moreover, the formed Ag nanodomains undergo alloying reaction with Li, followed by interdiffusion of both Ag and Li when Li is plated. This interdiffusion is reflected in the uniform distribution of Ag in the Li layer (Figure 4b) and simultaneously facilitates the homogeneous deposition of Li. The CEs of the same cells portrayed a consistent picture (Figure S8c, Supporting Information). The CE of the AgF-based electrode stabilized at comparably high levels (>99.5%) throughout 20 cycles whereas the CE of the Ag-based electrode remained low (≈98%) owing to the aforementioned agglomeration of Ag particles. Initially, the CE of the Ag/LiF-based electrode followed a similar track to that of its AgF counterpart,

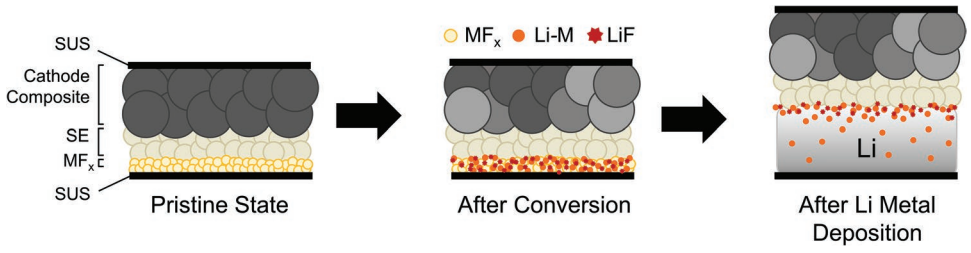

Figure 5. Schematic illustration of Li plating on MF_x-based electrode. Upon lithiation, metal fluoride (MF_x) undergoes a conversion reaction followed by Li plating in the bulk metallic form.

but deviated by decreasing at around the tenth cycle owing to the significant Ag agglomeration over the LiF barriers. The noteworthy inferior electrochemical performance of the Ag- and Ag/LiF-based electrodes compared to that of the AgF-based electrode emphasizes the importance of in situ conversion of AgF for a sustainable interface around Ag seeds.

2.6. Electrochemical Performance of Full Cells

The electrochemical performance of the AgF-based anode-less electrode was further investigated in a full-cell configuration at 25 °C by pairing it with a$LiNi_{0.8}Co_{0.1}Mn_{0.1}O_2$ (NCM811) cathode. The composite cathode was composed of NCM811:SE:vapor-grown carbon fiber (VGCF) = 70:28.5:1.5 by weight. We emphasize that the areal mass loading of NCM811 was controlled to be 50 mg cm^{-2}, a value far higher than that of current commercial LIBs, to warrant the competitive energy density of the cell. When cycled at 0.1 C (20 mA g_{NCM}^{-1}) for both charge and discharge, the AgF-based full cell delivered an exceptionally high areal capacity of 9.7 mAh cm^{-2} in the first cycle and maintained 85.4% of the original capacity after 50 cycles (**Figure 6**a; Figure S11, Supporting Information). As for the charge–discharge efficiency, the AgF-based full cell exhibited an initial CE of 90.1%, and this value rose to 99.1% at the third cycle. Afterward, the CE value steadily increased with cycling, resulting in an average CE of 99.5% for 50 cycles. The average CE between the 3rd and the 50th cycle was 99.7%. The long-term cycling performance of the AgF-based full cell is presented in Figure S12 (Supporting Information).

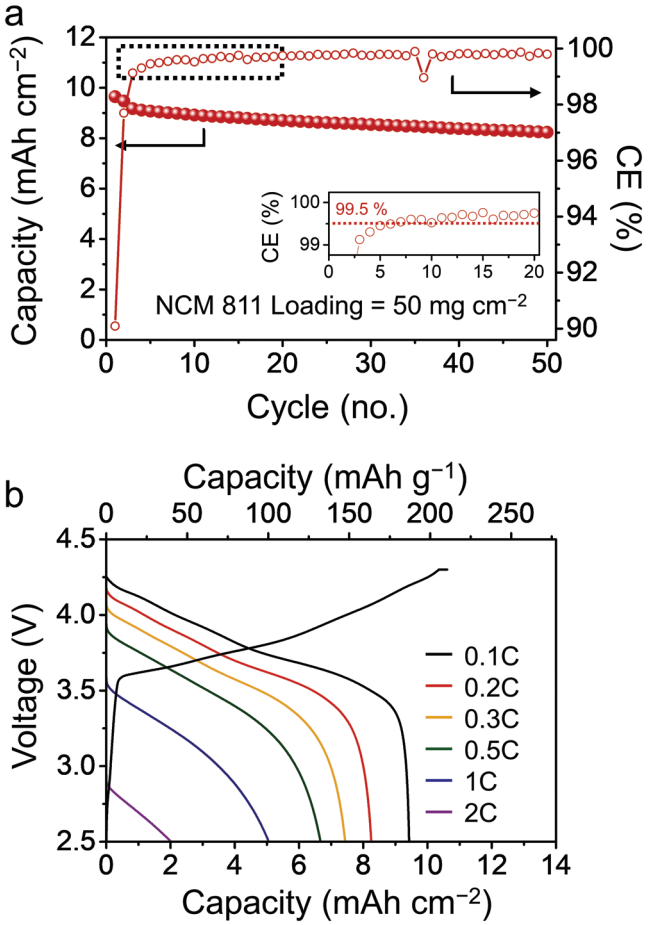

Figure 6. Electrochemical performance of AgF-based full cells. a) Cycling performance and CEs of NCM|SE|AgF all-solid-state full cell when tested at 0.1 C (20 mA g^{-1}) in the voltage range of 2.5–4.3 V at 25 °C. The areal loading of NCM811 active material = 50 mg cm^{-2}. The *C*-rate was defined as 1 C = 200 mA g_{NCM}^{-1}. b) Rate capability of the same cell when measured at various discharge *C*-rates. The charging rate was fixed at 0.1 C.

To see the change in the interfacial resistance during cycling, electrochemical impedance spectroscopy (EIS) analysis was carried out for the NCM|SE|AgF all-solid-state full cells before and after 1, 3, and 10 charge–discharge cycles (Figure S13, Supporting Information). The attained Nyquist plots were fitted to an equivalent circuit presented in Figure S13 (Supporting Information). The bulk resistance of SE (R_{SE}), and the charge-transfer resistance at the SE/cathode ($R_{SE/Cathode}$) and SE/anode ($R_{SE/Anode}$) interfaces were obtained from the *x*-axis intercept and the amplitudes of the semicircles in the medium and low-frequency regimes, respectively (Table S1, Supporting Information).[26] In the pristine state, the $R_{SE/Anode}$ of the cell was extremely high at 670.2 Ω cm^2 because AgF is not ionically conductive. After the first charging, the $R_{SE/Anode}$ dropped significantly to 9.0 Ω cm^2, but increased to 39.9 Ω cm^2 after the first discharging. After the third charging and discharging, the $R_{SE/Anode}$ increased slightly to 11.2 and 40.8 Ω cm^2, respectively. These values increased slightly further to 18.7 and 41.6 Ω cm^2, respectively at the tenth cycle. The series of data indicate that the $R_{SE/Anode}$ marked the highest at the pristine state, but decreased significantly during the initial conversion reaction and remained in the similar range thereafter. On the other hand, the effect of imposing the same charge/discharge conditions on the NCM|SE|Ag and NCM|SE|Ag/LiF full cells was that the voltage of both cells continued to charge without reaching the upper cutoff potential even in the first charging at 0.1 C after the formation cycles (Figure S14, Supporting Information) as a result of short-circuiting midway through the charge. This distinct charging stability again verifies the importance of uniform Li plating via well-distributed Ag seeds and the presence of insulating LiF, both of which jointly prevent Li plating from penetrating the SE layer toward soft shorting. For the same reason, a control full cell with the configuration NCM|SE|SUS had difficulty in raising the voltage even in the beginning of the first charge at 0.05 C (Figure S14g, Supporting Information) as the SUS electrode did not contain any nucleation seeds at all. The AgF-based full cell delivered decent rate performance upon variation of the discharge C rate from 0.1 to 2 C while the charge *C*-rate was fixed at 0.1 C considering its extraordinarily high loading of NCM811 (Figure 6b; Figure S15, Supporting Information).

3. Conclusion

In summary, the in situ conversion reaction of metal fluorides was exploited to enable sustainable cycling of anode-less sulfide-based ASSBs operating at room temperature. After a comparative analysis of various metal fluorides, AgF was identified to

be the most suitable option for the conversion reaction mainly because the metallic nanodomains resulting from this reaction lower the nucleation overpotential for the subsequent alloying reaction with Li, particularly by taking advantage of the solid-solution mechanism. Furthermore, LiF generated from the conversion reaction mitigates the indiscriminate growth of Li dendrites as well as agglomeration of metallic Ag nanodomains, leading to uniform and sustainable Li (de)plating over cycling even with an unparalleled high areal capacity of 9.7 mAh cm^{-2}. This systematic study widens the range of opportunities for advancing sulfide-based ASSBs to a more reliable and competitive level by offering a useful design principle for electrodes: microscopically distributed, reactive metallic domains in a stable matrix enable highly robust Li (de) plating.

4. Experimental Section

Materials: Aluminum fluoride (99%), silver(I) fluoride (98%), bismuth fluoride (99%), calcium fluoride (99.5%), cesium fluoride (99%), indium fluoride (96%), lithium fluoride (98.5%), magnesium fluoride (99%), tin(II) fluoride (97.5%), tin(IV) fluoride (99%), zinc fluoride (99%), and silver nanopowder (Ag NP, 99.9%) were purchased from Alfa-Aesar. The argyrodite $Li_6PS_5Cl_{0.5}Br_{0.5}$ with a particle size of 2 µm for the SE layer and 0.7 µm for the composite cathode was synthesized as reported previously.[11] PVDF with a weight-average molecular weight (M_w) of 560 000 g mol^{-1} was purchased from Sigma–Aldrich. *N*-methyl-2-pyrrolidone (NMP) was purchased from TCI Chemicals.

Cell Fabrication: The metal-fluoride-based electrodes were fabricated by preparing slurries consisting of 97.5 wt% of each metal fluoride and 2.5 wt% of PVDF binder in NMP at 40 °C, followed by casting on SUS foil and drying at 100 °C for 1 h and subsequently at 80 °C for 12 h. AgF was ball-milled at 650 rpm for 12 h before use, and other metal fluorides were used as received without ball-milling to ensure that the particle sizes are consistent among the samples. The areal mass loading of each metal fluoride layer was 0.25 mg cm^{-2}. The electrodes based on Ag and the Ag/LiF mixture were prepared by dispersing Ag NP or Ag NP:LiF = 1:1 in an atomic ratio with the binder in NMP in a weight ratio of 97.5:2.5, followed by the same casting and drying steps as above. Asymmetric MF_x|SE|Li half-cells were fabricated by first compressing the SE powder to a pellet at 110 MPa and positioning the premade anode-less composite layer on the SE pellet, followed by pressing the assembly at 490 MPa. After the compression, the anode-less electrode was transferred onto the SE pellet from the SUS foil. Next, Li metal and SUS foils were sequentially attached to the side of the pellet and compressed. The cell was then positioned in a housing case and tightened to 3 N m with a torque wrench. An external pressure of 20 MPa was applied during cell testing. The all-solid-state full cells were fabricated by preparing the anode-less composite layer via the same procedure as for the half-cells. The cathode composites were prepared by dry-mixing $LiNbO_3$-coated NCM811, SE, and VGCF in a weight ratio of 70:28.5:1.5 by using a centrifugal mixer (THINKY Inc.). The SE layer was prepared using the same procedure as for the half-cells. The cathode mixture and the anode-less composite layer were placed on either side of the SE pellet, and the whole assembly was then compressed at 490 MPa. The areal mass loading of NCM811 was 50 mg cm^{-2}. After compression, the cell was positioned in the same housing case as in the half-cell tests and tightened to 3 N m for cell testing. All the assembly processes were carried out in an Ar-filled glove box.

Electrochemical Characterization: The electrochemical performance of the anode-less|SE|Li all-solid-state half-cells was assessed using a battery cycler (WBCS3000L, WonATech). The current densities and areal capacities are noted in the legends of individual figures. The potential cutoff in the stripping process was 0.1 V. The electrochemical performance of the NCM|SE|anode-less all-solid-state full cells was assessed in constant current constant voltage (CCCV) mode for charge and constant current (CC) mode for discharge in the potential range of 2.5–4.3 V versus Li^+/Li using a battery cycler (MACCOR series 4000, Maccor). The cycling performance test was conducted by initially cycling the cells at a charging rate of 0.05 C and a discharging rate of 0.1 C for two cycles for the formation step, and then both charge and discharge proceeded at a constant *C*-rate of 0.1 C. In CCCV mode during charging, once the constant current charging reached 4.3 V, the voltage was held constant until the current density decreased to 0.05 C. For the rate performance test, the charge was unified at 0.1 C and the discharge was processed at various *C*-rates from 0.1 to 2 C. All the electrochemical measurements were carried out at 25 °C. The interfacial resistances of the NCM|SE|anode-less all-solid-state full cells were measured by EIS using a battery cycler (VSP, Bio-Logic) in the frequency range from 1 MHz to 0.1 Hz. The obtained impedance profiles were fitted to the equivalent circuit using the Z-view software. The ionic conductivity of the SE was calculated from the relation of $\sigma = L/R_b\ A$ (where L is the thickness of the SE layer, R_b is the bulk resistance of SE, and A is the area of the SE layer). The ionic conductivity of the SE used was 4.5 mS cm^{-1} according to the impedance analysis of the SUS|SE|SUS symmetric cell.

Materials' Characterization: The changes in the chemical compositions of AgF and InF_3 upon lithiation were analyzed by XPS (Nexsa, Thermo Fisher Scientific). The changes in the crystal structures of AgF and InF_3 before and after Li plating were examined by performing XRD analysis (New D8 Advance, Bruker). The bonding characteristics of the SE were analyzed using Raman spectroscopy (Raman; DXR2xi, Thermo). The XRD and Raman spectra of the SE used are provided in Figure S16 (Supporting Information). The high-resolution scanning transmission electron microscopy (STEM) images of AgF after the conversion reaction were acquired using Cs-corrected STEM (JEM-ARM200F, Jeol). The top-view images of the AgF- and Ag/LiF-based electrodes were obtained using SEM (SEM-7800F Prime, Jeol). The cross-sectional images of the AgF-based electrodes before and after cycling were acquired using SEM (JSM-7610FPlus, Jeol) after dicing the cells with a cross-section polisher (CP; ArBlade 5000, Hitachi). Elemental mapping was conducted with EDS (Ultim Extreme, Oxford Instruments).

Supporting Information

Supporting Information is available from the Wiley Online Library or from the author.

Acknowledgements

The authors acknowledge support from the Swiss National Science Foundation (SNF) (grant No. Singergia CRSII5_202296), the National Research Foundation of Korea (NRF) (Grant Nos. 2021R1A2B5B03001956, NRF-2021M3H4A3A02086210, and NRF-2022M3J1A1054151) and generous support from the Institute of Engineering Research (IOER) and Research Institute of Advanced Materials (RIAM) at Seoul National University.

Conflict of Interest

The authors declare no conflict of interest.

Data Availability Statement

The data that support the findings of this study are available from the corresponding author upon reasonable request.

Keywords

all-solid-state batteries, anode-less batteries, argyrodite, conversion, metal fluorides

Received: April 20, 2022
Revised: July 31, 2022
Published online: September 1, 2022

[1] a) J. Janek, W. G. Zeier, *Nat. Energy* **2016**, *500*, 300; b) D. Cao, Y. Zhao, X. Sun, A. Natan, Y. Wang, P. Xiang, W. Wang, H. Zhu, *ACS Energy Lett.* **2020**, *5*, 3468; c) L. Xu, Y. Lu, C.-Z. Zhao, H. Yuan, G.-L. Zhu, L.-P. Hou, Q. Zhang, J.-Q. Huang, *Adv. Energy Mater.* **2020**, *11*, 2002360; d) Q. Zhao, S. Stalin, C.-Z. Zhao, L. A. Archer, *Nat. Rev. Mater.* **2020**, *5*, 229; e) J. Lee, T. Lee, K. Char, K. J. Kim, J. W. Choi, *Acc. Chem. Res.* **2021**, *54*, 3390; f) J. Wu, L. Shen, Z. Zhang, G. Liu, Z. Wang, D. Zhou, H. Wan, X. Xu, X. Yao, *Electrochem. Energy Rev.* **2021**, *4*, 101; g) J. Wu, S. Liu, F. Han, X. Yao, C. Wang, *Adv. Mater.* **2021**, *33*, 2000751.

[2] a) Y. Inaguma, C. Liquan, M. Itoh, T. Nakamura, T. Uchida, H. Ikuta, M. Wakihara, *Solid State Commun.* **1993**, *86*, 689; b) Y. S. Jung, D. Y. Oh, Y. J. Nam, K. H. Park, *Isr. J. Chem.* **2015**, *55*, 472; c) T. Asano, A. Sakai, S. Ouchi, M. Sakaida, A. Miyazaki, S. Hasegawa, *Adv. Mater.* **2018**, *30*, 1803075.

[3] a) L. Zhou, N. Minafra, W. G. Zeier, L. F. Nazar, *Acc. Chem. Res.* **2021**, *54*, 2717; b) Z. Zhang, L. Wu, D. Zhou, W. Weng, X. Yao, *Nano Lett.* **2021**, *21*, 5233; c) G. Liu, J. Shi, M. Zhu, W. Weng, L. Shen, J. Yang, X. Yao, *Energy Storage Mater.* **2021**, *38*, 249.

[4] L. Zhou, A. Assoud, Q. Zhang, X. Wu, L. F. Nazar, *J. Am. Chem. Soc.* **2019**, *141*, 19002.

[5] Y. Kato, S. Hori, T. Saito, K. Suzuki, M. Hirayama, A. Mitsui, M. Yonemura, H. Iba, R. Kanno, *Nat. Energy* **2016**, *1*, 16030.

[6] N. Kamaya, K. Homma, Y. Yamakawa, M. Hirayama, R. Kanno, M. Yonemura, T. Kamiyama, Y. Kato, S. Hama, K. Kawamoto, A. Mitsui, *Nat. Mater.* **2011**, *10*, 682.

[7] a) K. Lee, J. Lee, S. Choi, K. Char, J. W. Choi, *ACS Energy Lett.* **2018**, *4*, 94; b) J. Lee, K. Lee, T. Lee, H. Kim, K. Kim, W. Cho, A. Coskun, K. Char, J. W. Choi, *Adv. Mater.* **2020**, *32*, 2001702.

[8] a) J. Wu, L. Yuan, W.-X. Zhang, Z. Li, X. Xie, Y. Huang, *Energy Environ. Sci.* **2020**, *14*, 12; b) J. Lee, J. W. Choi, *Ecomat* **2022**, *4*, e12193.

[9] Y.-S. Hu, *Nat. Energy* **2016**, *1*, 16042.

[10] a) J. M. Whiteley, S. Hafner, C. Zhu, W. Zhang, S.-H. Lee, *J. Electrochem. Soc.* **2017**, *164*, A2962; b) C. Yang, L. Zhang, B. Liu, S. Xu, T. Hamann, D. McOwen, J. Dai, W. Luo, Y. Gong, E. D. Wachsman, L. Hu, *Proc. Natl. Acad. Sci. USA* **2018**, *115*, 3770; c) X. Ji, S. Hou, P. Wang, X. He, N. Piao, J. Chen, X. Fan, C. Wang, *Adv. Mater.* **2020**, *32*, 2002741; d) A. Paolella, X. Liu, A. Daali, W. Xu, I. Hwang, S. Savoie, G. Girard, A. G. Nita, A. Perea, H. Demers, W. Zhu, A. Guerfi, A. Vijh, G. Bertoni, G. C. Gazzadi, G. Berti, C. Sun, Y. Ren, K. Zaghib, M. Armand, C. Kim, G.-L. Xu, K. Amine, *Adv. Funct. Mater.* **2021**, *31*, 2102765; e) Y.-K. Sun, P. V. Kamat, *ACS Energy Lett.* **2021**, *6*, 2356.

[11] D. J. Yoo, A. Elabd, S. Choi, Y. Cho, J. Kim, S. J. Lee, S. H. Choi, T. W. Kwon, K. Char, K. J. Kim, A. Coskun, J. W. Choi, *Adv. Mater.* **2019**, *31*, 1901645.

[12] a) A. Banerjee, X. Wang, C. Fang, E. A. Wu, Y. S. Meng, *Chem. Rev.* **2020**, *120*, 6878; b) T. Krauskopf, F. H. Richter, W. G. Zeier, J. Janek, *Chem. Rev.* **2020**, *120*, 7745.

[13] a) S. Wenzel, S. J. Sedlmaier, C. Dietrich, W. G. Zeier, J. Janek, *Solid State Ionics* **2018**, *318*, 102; b) F. Han, J. Yue, X. Zhu, C. Wang, *Adv. Energy Mater.* **2018**, *8*, 1703644; c) Y. Zhou, C. Doerrer, J. Kasemchainan, P. G. Bruce, M. Pasta, L. J. Hardwick, *Batteries Supercaps* **2020**, *3*, 647; d) D. S. Jolly, Z. Ning, G. O. Hartley, B. Liu, D. L. R. Melvin, P. Adamson, J. Marrow, P. G. Bruce, *ACS Appl. Mater. Interfaces* **2021**, *13*, 22708.

[14] a) J. Schnell, T. Günther, T. Knoche, C. Vieider, L. Köhler, A. Just, M. Keller, S. Passerini, G. Reinhart, *J. Power Sources* **2018**, *382*, 160; b) W. Ping, C. Wang, Z. Lin, E. Hitz, C. Yang, H. Wang, L. Hu, *Adv. Energy Mater.* **2020**, *10*, 2000702; c) B. Wu, S. Wang, W. J. EvansIV, D. Z. Deng, J. Yang, J. Xiao, *J. Mater. Chem. A* **2016**, *4*, 15266; d) S. Narayanan, J. S. Gibson, J. Aspinall, R. S. Weatherup, M. Pasta, *Curr. Opin. Solid State Mater. Sci.* **2022**, *26*, 100978.

[15] a) J. Qian, B. D. Adams, J. Zheng, W. Xu, W. A. Henderson, J. Wang, M. E. Bowden, S. Xu, J. Hu, J. G. Zhang, *Adv. Funct. Mater.* **2016**, *26*, 7094; b) K. Yan, Z. Lu, H.-W. Lee, F. Xiong, P.-C. Hsu, Y. Li, J. Zhao, S. Chu, Y. Cui, *Nat. Energy* **2016**, *1*, 16010; c) X. Ren, L. Zou, X. Cao, M. H. Engelhard, W. Liu, S. D. Burton, H. Lee, C. Niu, B. E. Matthews, Z. Zhu, C. Wang, B. W. Arey, J. Xiao, J. Liu, J.-G. Zhang, W. Xu, *Joule* **2019**, *3*, 1662; d) Z. Xie, Z. Wu, X. An, X. Yue, J. Wang, A. Abudula, G. Guan, *Energy Storage Mater.* **2020**, *32*, 386; e) C. Heubner, S. Maletti, H. Auer, J. Hüttl, K. Voigt, O. Lohrberg, K. Nikolowski, M. Partsch, A. Michaelis, *Adv. Funct. Mater.* **2021**, *31*, 2106608; f) L. Lin, L. Suo, Y. s. Hu, H. Li, X. Huang, L. Chen, *Adv. Energy Mater.* **2021**, *11*, 2003709; g) O. Tamwattana, H. Park, J. Kim, I. Hwang, G. Yoon, T.-h. Hwang, Y.-S. Kang, J. Park, N. Meethong, K. Kang, *ACS Energy Lett.* **2021**, *6*, 4416; h) Y. Liu, X. Wu, C. Niu, W. Xu, X. Cao, J.-G. Zhang, X. Jiang, J. Xiao, J. Yang, M. S. Whittingham, J. Liu, *ACS Energy Lett.* **2021**, *6*, 1550; i) C. Wang, M. Liu, M. Thijs, F. G. Ooms, S. Ganapathy, M. Wagemaker, *Nat. Commun.* **2021**, *12*, 6536.

[16] Y.-G. Lee, S. Fujiki, C. Jung, N. Suzuki, N. Yashiro, R. Omoda, D.-S. Ko, T. Shiratsuchi, T. Sugimoto, S. Ryu, J. H. Ku, T. Watanabe, Y. P. Park, Y. Aihara, D. Im, I. T. Han, *Nat. Energy* **2020**, *5*, 299.

[17] Q. Pang, X. Liang, I. R. Kochetkov, P. Hartmann, L. F. Nazar, *Angew. Chem., Int. Ed.* **2018**, *57*, 9795.

[18] a) F. Li, Y.-H. Tan, Y.-C. Yin, T.-W. Zhang, L.-L. Lu, Y.-H. Song, T. Tian, B. Shen, Z.-X. Zhu, H.-B. Yao, *Chem. Sci.* **2019**, *10*, 9735; b) R. Pathak, K. Chen, A. Gurung, K. M. Reza, B. Bahrami, J. Pokharel, A. Baniya, W. He, F. Wu, Y. Zhou, K. Xu, Q. Qiao, *Nat. Commun.* **2020**, *11*, 93.

[19] a) J. T. Wolan, G. B. Hoflund, *Appl. Surf. Sci.* **1998**, *125*, 251; b) D. Jiang, X. Du, Q. Liu, L. Zhou, L. Dai, J. Qian, K. Wang, *Analyst* **2015**, *140*, 6404.

[20] a) G. Schön, J. Tummavuori, B. Lindström, C. Enzell, C. Enzell, C. Swahn, *Acta Chem. Scand.* **1973**, *27*, 2623; b) M. Wagstaffe, H. Hussain, M. J. Acres, R. Jones, K. L. Syres, A. G. Thomas, *J. Phys. Chem. C* **2017**, *121*, 21383.

[21] a) G. Taillades, J. Sarradin, *J. Power Sources* **2004**, *125*, 199; b) S. Zhang, G. Yang, Z. Liu, S. Weng, X. Li, X. Wang, Y. Gao, Z. Wang, L. Chen, *ACS Energy Lett.* **2021**, *6*, 4118.

[22] J. Wan, Y.-X. Song, W.-P. Chen, H.-J. Guo, Y. Shi, Y.-J. Guo, J.-L. Shi, Y.-G. Guo, F.-F. Jia, F.-Y. Wang, R. Wen, L.-J. Wan, *J. Am. Chem. Soc.* **2020**, *143*, 839.

[23] a) B. Sun, J. Lang, K. Liu, N. Hussain, M. Fang, H. Wu, *Chem. Commun.* **2019**, *55*, 1592; b) A. Santhosha, L. Medenbach, J. R. Buchheim, P. Adelhelm, *Batteries Supercaps* **2019**, *2*, 524.

[24] S. Jin, Y. Ye, Y. Niu, Y. Xu, H. Jin, J. Wang, Z. Sun, A. Cao, X. Wu, Y. Luo, H. J. Ji, L.-J. Wan, *J. Am. Chem. Soc.* **2020**, *142*, 8818.

[25] F. Wang, H.-C. Yu, M.-H. Chen, L. Wu, N. Pereia, K. Thornton, A. Van der Ven, Y. Zhu, G. G. Amatucci, J. Graetz, *Nat. Commun.* **2012**, *3*, 1201.

[26] a) D. Y. Oh, D. H. Kim, S. H. Jung, J.-G. Han, N.-S. Choi, Y. S. Jung, *J. Mater. Chem. A* **2017**, *5*, 20771; b) Z. Zhang, L. Zhang, Y. Liu, C. Yu, X. Yan, B. Xu, L.-m. Wang, *J. Alloys Compd.* **2018**, *747*, 227.